Nanoscale Horizons

ROYAL SOCIETY OF CHEMISTRY

COMMUNICATION

View Article Online
View Journal

Cite this: DOI: 10.1039/d5nh00763a

Received 20th November 2025,
Accepted 10th April 2026

DOI: 10.1039/d5nh00763a

rsc.li/nanoscale-horizons

Detecting conformational changes in switchable heterodimer plasmon rulers through iSCAT fluctuation microscopy

Aidan Oi, Koustav Kundu, Ritesh K. Bag and Björn M. Reinhard *

The superb detection sensitivity of interferometric scattering (iSCAT) microscopy enables a high-speed optical read-out of individual dimers of DNA-tethered noble metal nanoparticles (NPs), so called Plasmon Rulers. The iSCAT contrast of Plasmon Rulers depends on their structure, and fluctuations of the iSCAT contrast may provide insight into the conformational dynamics of the tether molecule. In this work, heterodimer Plasmon Rulers are assembled from 40 and 20 nm diameter Au NPs using a switchable DNA tether. The tether contains a central molecular beacon hairpin sequence that opens upon binding of the micro-RNA (miRNA) 574-3P (M_W = 6582.3 Da). The 40 nm NP of the heterodimers is immobilized on a glass support, while the 20 nm NP is left to perform a tethered particle diffusion. The iSCAT contrast of individual heterodimers is collected before and after exposure to miRNA with an acquisition rate of 50 kHz. Binding of the 22 nucleotides long target miRNA to the molecular beacon segment increases the accessible conformational space of the tethered 20 nm NP. The resulting gain in conformational variability of the heterodimer is detected as a significant increase in the mean absolute deviation (MAD) of the iSCAT contrast. These findings confirm that iSCAT fluctuation microscopy of the heterodimer Plasmon Rulers can detect conformational changes in the tether molecule and pave the path to monitoring the conformational dynamics of individual biopolymers.

New concepts

This work demonstrates that Plasmon Ruler heterodimers comprising 40 nm and 20 nm Au NPs linked by a DNA tether in combination with iSCAT fluctuation microscopy facilitate the detection of small (22 nucleotides) RNA targets. A tether strand containing a molecular beacon motif changes its length upon binding of the target micro-RNA (miRNA), and this event becomes detectable as an increase in iSCAT signal fluctuation due to the orientation- and interparticle separation-dependent iSCAT signal of the heterodimer. More fundamentally, this study highlights the wealth of information that becomes accessible by characterizing the structural dynamics of plasmonic molecules using iSCAT fluctuation microscopy. Especially since the heterodimer approach achieves a reduction of steric perturbations compared to Plasmon Ruler homodimers assembled from 40 nm Au NPs, this approach paves a path to a nanoscale tethered bead assay with reduced steric perturbation that can characterize the structural dynamics of even small biomolecules.

Introduction

Plasmon Rulers are discrete dimers of polymer-tethered noble metal nanoparticles (NPs) that utilize shifts of the far-field scattering spectrum associated with the distance-dependent coupling of localized plasmons in metal NPs as a read-out to monitor nanometer-scale distances.[1–4] The distance-dependence of the scattering spectrum of discrete NP dimers has been characterized experimentally for both Au[5,6] and Ag[7] NPs. In the electromagnetic coupling regime the spectral shift $\Delta\lambda$ as a function of the edge-to-edge separation s between the NPs is well described by a universal scaling relation that depends on the monomer resonance wavelength λ_0, the NP diameter D, as well as the amplitude a and decay constant τ:[8]

$$\frac{\Delta\lambda}{\lambda_0} = a\exp\left(-\frac{s/D}{\tau}\right) \quad (1)$$

The interparticle separation dependent scattering signal in combination with the photophysical stability of the NP probes make individual Plasmon Rulers an experimental platform for monitoring structural fluctuations in the tether molecule with high temporal resolution and no limitations in observation time.[9–12] In addition to polymer-tethered homodimers, heterodimers assembled from NPs with different sizes and shapes have also been examined for Plasmon Ruler applications.[13,14] In this case, the scattering signal of a larger immobilized NP is modulated through the motion of a smaller polymer-tethered NP. Visser *et al.*[13] demonstrated through combination of Brownian dynamics and electromagnetic simulations that heterodimer Plasmon Rulers have promise for detecting rapid structural fluctuation in the tether molecule. A reduction in

Department of Chemistry and The Photonics Center, Boston University, Boston, MA 02215, USA. E-mail: bmr@bu.edu

the size of the NP performing the tethered particle motion reduces (i) excluded volume and steric effects, (ii) the excursion number of the system,[15,16] $N_R = \frac{R}{\sqrt{L\xi/3}}$, where R is the radius of the diffusing NP, L the contour length, and ξ the persistence length of the tether molecule, (iii) the risk of multivalent contacts, and (iv) the NP relaxation time.[17] The latter is given as a ratio of viscous drag coefficient and tether stiffness and limits the maximum temporal resolution of the tethered NP assay.[18] N_R is a relationship between the radius of the tethered NP and the tether stiffness and represents a metric to ascertain whether the tethered particle motion is dominated by the tether ($N_R < 1$) or particle motion ($N_R > 1$).[15] According to the definition of the excursion number, a decrease in the radius of the tethered NPs in Plasmon Rulers facilitates a reduction in the tether length that can be investigated without risk of perturbing the statistical properties of the molecule.

While the outlined effects i–iv are generally favorable for smaller NP sizes, one caveat is that the effect of the diffusing NP motion on the scattering signal of the heterodimer decreases with NP size. In most prior Plasmon Ruler studies darkfield microscopy was applied to detect the elastic scattering signal of the coupled NPs.[19,20] Recently, it was shown that interferometric scattering (iSCAT) microscopy provides an alternative strategy for monitoring plasmon coupling in discrete assemblies of NPs, including those assembled from NPs with sizes that are no longer detectable by conventional darkfield microscopy.[21–27] iSCAT microscopy is a common path interferometric imaging strategy in which the light scattered from an object of interest interferes with a reflected reference beam in the plane of detection.[28–30] The iSCAT signal, I_{iscat}, has contributions from reflection, scattering and interference of both:[29,31]

$$I_{iSCAT} \propto |E_{ref}|^2 + |E_{scat}|^2 + 2|E_{ref}|\,|E_{scat}|\cos(\phi) \qquad (2)$$

In this expression E_{ref} and E_{scat} are the complex reflected and scattered fields and ϕ the phase between reference and scattered beam. Close to the plasmon resonance the scattering cross-section and phase of a NP scatterer are strongly wavelength dependent (Fig. S1).[32,33] Consequently, shifts in the coupled plasmon resonance of DNA-tethered NP dimers due to distance-dependent electromagnetic interactions alter the wavelength-dependent scattering cross-section and phase to modulate the iSCAT contrast that is detected in the far-field. We previously used this approach to characterize thermal structural fluctuations in polymer-tethered assemblies of 10 nm and 20 nm Ag NPs and demonstrated detectable fluctuations in the iSCAT contrast monitored at discrete wavelengths around the NP plasmon resonance.[21] In this work we set out to experimentally characterize the iSCAT signal

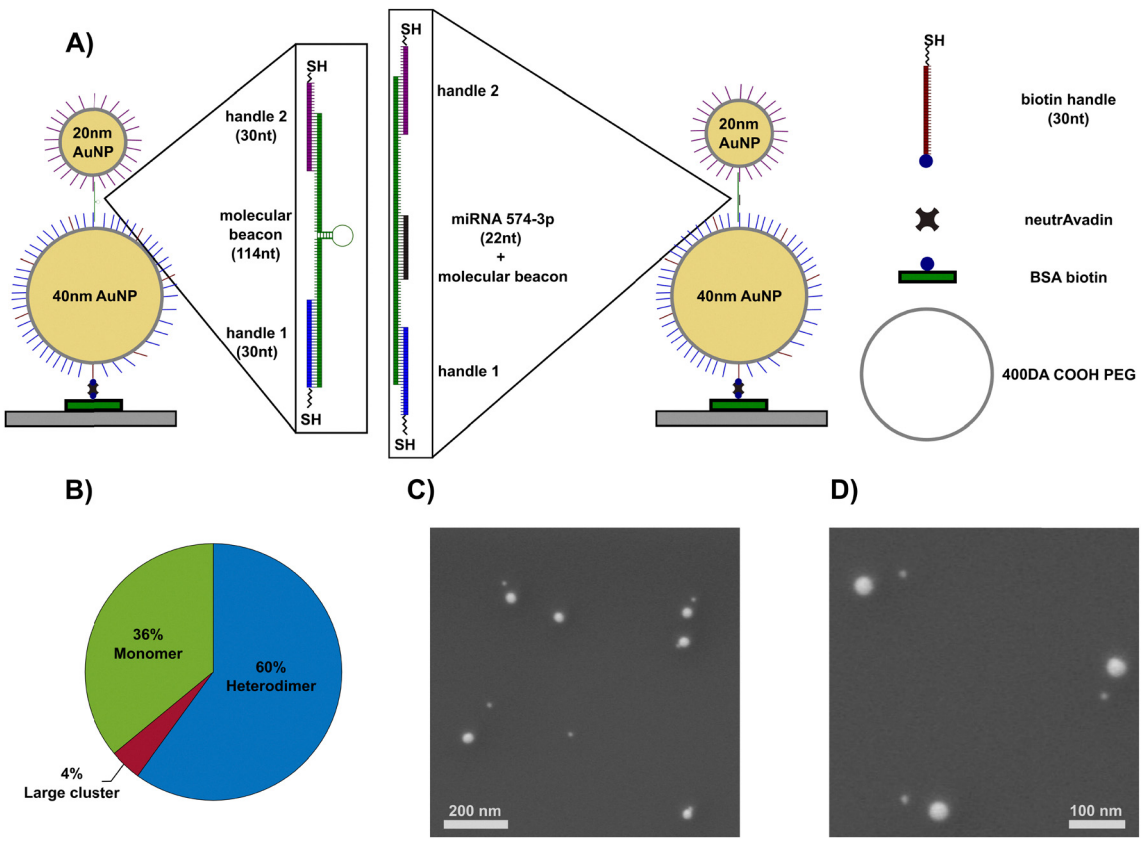

Fig. 1 (A) Scheme of the 40 nm/20 nm Au NP heterodimer Plasmon Ruler for the open and closed molecular beacon. (B) Contributions from 40 nm monomers, heterodimers, and larger clusters to Plasmon Ruler sample as determined by SEM. (C and D) SEM images of 40 nm/20 nm Au NP heterodimers.

fluctuations associated with tethered particle motion in individual heterodimer Plasmon Rulers consisting of a 20 nm Au NP linked by a switchable DNA tether to an immobilized 40 nm Au NP and examined whether conformational changes in the tether can be detected. To that end, we integrated a molecular beacon like DNA sequence[34–37] that recognizes a 22 nucleotide long micro RNA (miRNA) into the DNA tether and characterized the signal fluctuations before and after addition of the miRNA. Binding of the target opens the hairpin of the molecular beacon like sequence and induces an increase in the end-to-end length of the tether molecule. We provide evidence that a miRNA binding-induced opening of the hairpin in the tether strand results in a statistically significant increase in the fluctuations of the detected time-dependent iSCAT signal. This finding is rationalized by an increase in the accessible conformational space of the tethered NP after target miRNA binding. Consequently, the tethered NP explores more structural conformations with different degrees of plasmon coupling, and this increased variability in plasmon coupling translates into increased fluctuations of the detected iSCAT signal.

Results and discussion

The design of the DNA-linked 40 nm/20 nm Au NP heterodimer under investigation in this work is shown in Fig. 1A. The 40 nm Au NP is immobilized on the glass substrate using established biotin-NeutrAvidin chemistry, but the 20 nm NPs lack biotin functionalization and perform a tethered NP motion in solution. The tether molecule contains a central molecular beacon element that in the absence of a complementary miRNA is folded into a hairpin structure. This structure is flanked by single stranded DNA linkers whose ends are complementary to the handles bound to the Au NPs to facilitate integration into the dimer. Binding of the target miRNA opens the DNA hairpin and extends the DNA. Worm-like-chain (WLC) modelling of the tether strand predicts end-to-end distances of 14.6 nm and 17.2 nm before and after miRNA binding.[38] The target chosen in this work, miRNA 574-3P, is a biomarker for prostate cancer that can be collected non-invasively *via* urine samples.[39,40] We picked this particular miRNA for our proof-of-principle study as the recognizant molecular beacon sequence is well tested and characterized.[41] One important aspect to note is that the DNA-linked 40 nm/20 nm Au NP heterodimer has excursion numbers of $N_R = 0.66$ and $N_R = 0.51$ for the closed and open states of the molecular beacon sequence in the tether. Both conditions are consequently expected to be dominated by the motion of the tether. In contrast, a 40 nm Au NP homodimer would have excursion numbers of $N_R = 1.32$ and $N_R = 1.02$ for the closed and open states, which lie in the range of NP-dominated motion.

The heterodimers were assembled following a DNA-programmed self-assembly protocol established for homodimers[6,9] with slight adjustments (see Methods). Dynamic light scattering (DLS) data of NPs at different steps of the dimer assembly process (Table S1) show a systematic increase in hydrodynamic diameter along the following preparation steps: citrate-stabilized NPs, BSPP-functionalized NPs, DNA-functionalized NP monomers, DNA-tether-linked NP dimers. The *z*-average of the hydrodynamic diameter of the combined solution was 117.4 ± 4.2 nm, and thus larger than the sum of the diameters of DNA functionalized 40 nm NPs (47.5 ± 0.2 nm) and molecular beacon functionalized 20 nm NPs (27.0 ± 0.6 nm), indicating formation of a mix of heterodimers and larger assemblies. UV-VIS spectra (Fig. S2) confirmed a slight red-shift and broadening of the LSPR peak, consistent with the formation of DNA-tethered NP assemblies. To isolate NP heterodimers from the mix, gel-electrophoresis was performed. Fig. S3 shows the image of an agarose gel containing 40 and 20 nm Au NP monomers functionalized with handles as well as a mix of the two with addition of the molecular beacon DNA tether. The gel shows a new and slower band in the presence of the molecular beacon DNA that indicates the successful formation of heterodimers. Scanning electron microscopy (SEM) imaging of the particles retrieved from the dimer band in the gel confirm an enrichment of heterodimers (Fig. 1B–D). We found that the recovered band contains 60% heterodimers, 36% monomers, and 4% larger aggregates. The spatial separation between the 20 and 40 nm NPs of many discrete heterodimers and the lack of homodimers in the SEM images (Fig. 1C and D) further confirms a specific tethering through the DNA linker rather than non-specific attachment.

The gel-purfied and isolated heterodimers were immobilized on a glass slide that formed the bottom of a flow cell *via* the biotin functionalized 40 nm Au NPs and then transferred into an iSCAT microscope (Fig. S4A). The emission from a 520 nm laser diode was circularly polarized and focused into the sample plane using a 100× NA = 1.3 objective. To locate NP scatterers, the sample was scanned in a raster pattern under a stationary laser beam. The light reflected from the glass/water interface and scattered by NPs was collected by the same objective and imaged with a photodetector. A representative iSCAT image of a single 40 nm Au NP obtained in the set-up as well a signal variance map of a 40 nm/20 nm Au NP heterodimer are included in Fig. S4B–D. For iSCAT signal fluctuation measurements, the photodetector collected the iSCAT signal (I_{iSCAT}) in the center of the point-spread-function of each scattering object with a sampling rate of $f = 50$ kHz for a total of 20 s. We chose the acquisition time $1/f = 20$ μs as a compromise between temporal resolution and signal-to-noise. Raw signal trajectories for representative 40 nm/20 nm heterodimers and 40 nm NP monomers, as well as for background and dark count measurements are provided in Fig. S5. For each NP or heterodimer iSCAT trajectory, a background trajectory in an adjacent region void of any NP scatterer was recorded. The average background signal I_{ref} was used to determine the iSCAT contrast σ_{iSCAT} at each timepoint i:

$$\sigma_{iSCAT}(i) = \frac{I_{iSCAT}(i) - I_{ref}}{I_{ref}} \quad (3)$$

We collected iSCAT contrast trajectories for individual NP scatterers before and after addition of a 100 nM miRNA solution. At the end of the experiment we added a 10 mM

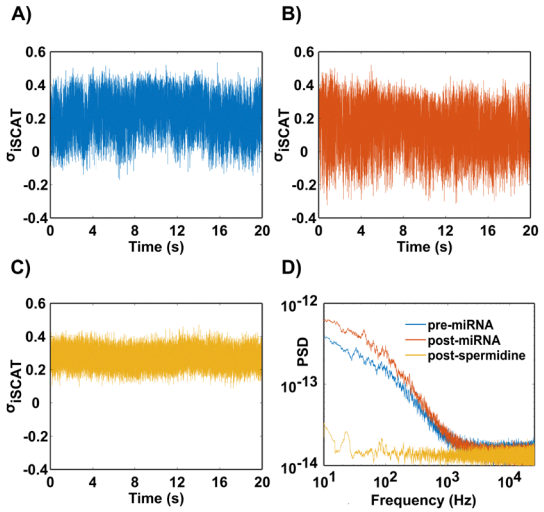

Fig. 2 (A) iSCAT contrast in T50 buffer before the addition of miRNA recorded with a sampling rate of 50 kHz. (B) iSCAT contrast after the addition of 100nM complementary miRNA sequence. (C) iSCAT contrast post 10 mM spermidine. (D) The power spectral densities of a single dimer for the three different conditions. Data shown are 50 points sliding averages in (A)–(C) and 100 points sliding average in (D).

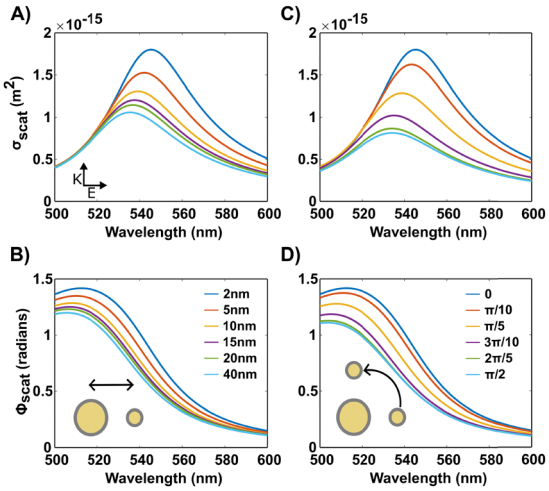

Fig. 3 Scattering cross-section (top row) and phase plots (bottom row) for 40 nm/20 nm Au NP heterodimers as function of interparticle separation (edge-to-edge) (A and B) and orientation of the dimer axis with respect to the incident *E*-field (C and D) calculated with a pairpolarizability model in the quasistatic approximation.

solution of the polyamine spermidine. The polycation binds to the negative DNA phosphate backbone and connects different locations of the DNA or DNA/miRNA hybrid, which results in a collapse and immobilization of the nucleic acid tether.[42–44] Overall, iSCAT data was obtained for dimers under four different conditions, referred to in the following as pre-miRNA before any miRNA has been introduced, post-NCmiRNA after 100 nM of the non-complementary miRNA sequence was added as a negative control, post-miRNA after 100 nM of the complementary sequence miRNA 574-3P was added, and post-spermidine after the incorporation of 10 mM spermidine. σ_{iSCAT} trajectories for one heterodimer scatterer under pre-miRNA, post-miRNA, and post-spermidine conditions are shown in Fig. 2A–C. One difference between the three experimental conditions that is immediately obvious is that the variance of the iSCAT contrast after collapse of the tether through spermidine is much smaller than for the heterodimer pre-miRNA or post-miRNA. Power-spectral density (psd) plots of the three conditions in Fig. 2D provide further evidence for this difference. Before the collapse of the nucleic acid tether, the tethered diffusion of the 20 nm NP in the heterodimer continuously changes the interparticle separation and relative orientation of the two NPs in the heterodimer. These structural fluctuations affect the plasmon coupling between the NPs and thus the scattering spectrum and phase of the dimer[45] (Fig. 3). Since both the scattering cross-section and phase affect the iSCAT signal according to eqn (2), the diffusion of the tethered 20 nm NP results in a modulation of the iSCAT contrast σ_{iSCAT}. According to the pair polarizability model in Fig. 3 it appears that the coupling primarily affect the phase component of the iSCAT signal in eqn (2). The pair polarizability model accounts, however, only for the dipolar coupling between the Au NPs and does not include quadrupole and higher order angular momentum interactions. The model therefore likely underestimates spectral and phase shifts associated with coupling and their effects on the iSCAT signal. The collapse of the DNA through addition of the spermidine immobilizes the tethered 20 nm NP, and the obvious decrease in iSCAT contrast fluctuations in this case is a direct consequence of the loss of structural dynamics in the heterodimer. Some trajectories showed increased fluctuations in a frequency range at around 90 Hz, which was particularly prominent in the otherwise relatively low-noise trajectories of spermidine aggregated dimers (Fig. S6). These fluctuations were, however, an experimental artifact and did not affect the interpretation of the data.

The PSD plots in Fig. 2D indicate a higher degree of σ_{iSCAT} fluctuations for the heterodimer after addition of miRNA. To test whether this smaller change is statistically significant in a larger sample size, we examined the contrast fluctuations for ~100 heterodimer Plasmon Rulers for the pre-miRNA, post-miRNA, and post-spermidine conditions, as well as for 40 nm Au NP monomers and post-NCmiRNA heterodimers as controls. Fig. 4A and B summarize the mean absolute deviation (MAD), defined as the average absolute difference between each data point and the median of the trajectory, as a metric to systematically compare fluctuations in σ_{iSCAT} for individual heterodimers and NPs and the two-sided Student t test results for the investigated conditions. We applied a 50-point sliding average to the σ_{iSCAT} data recorded at 50 kHz prior to the MAD analysis, as the heterodimer PSD plots drop to the baseline of the spermidine-compacted dimers and NP monomers (Fig. S7) for higher frequencies. The post-miRNA condition has a significantly higher average MAD and much broader distribution than the other investigated heterodimer and monomer conditions in Fig. 4A and B. The post-miRNA MAD distribution partially overlaps with the pre-miRNA and post-NCmiRNA data but also has an obvious tail with higher MAD. Overall, the post-miRNA

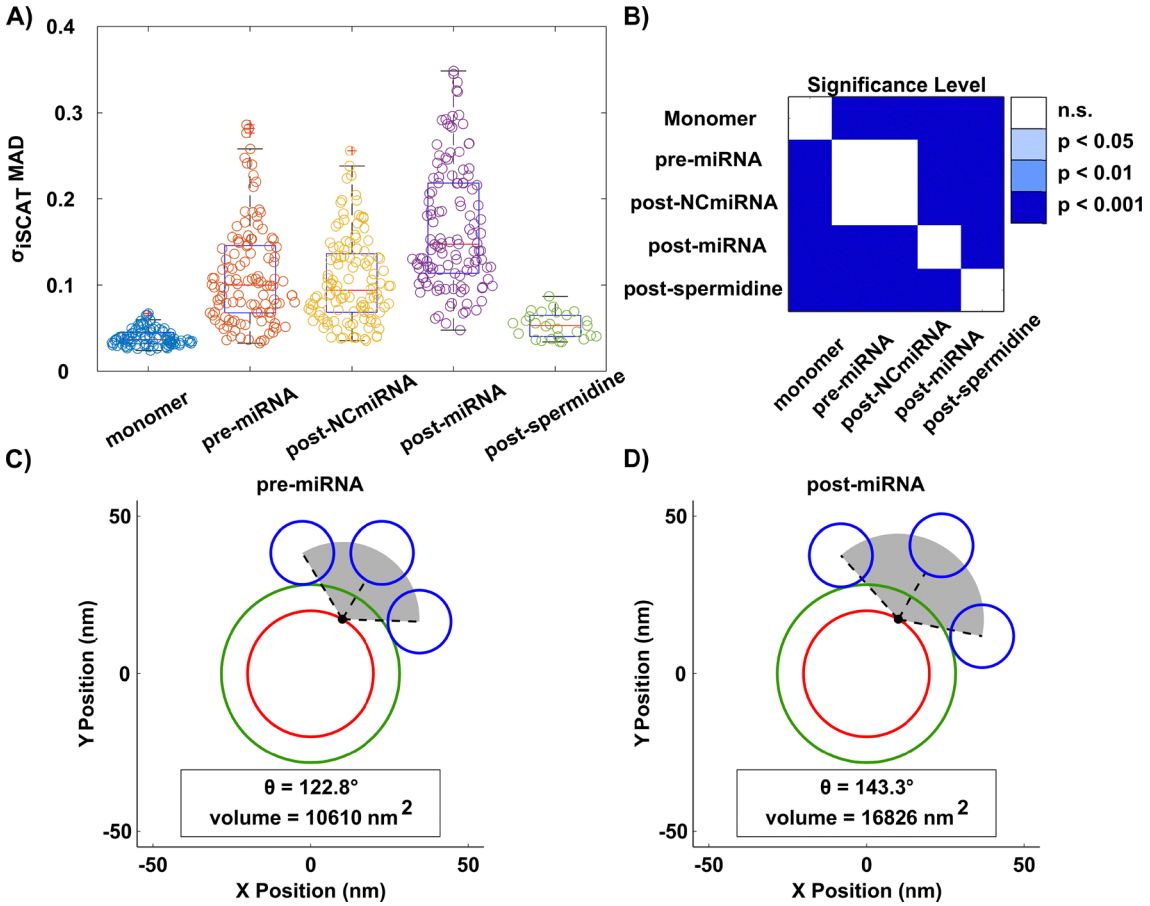

Fig. 4 (A) Comparison of the mean absolute deviation (MAD) of the iSCAT contrast for 40 nm/20 nm Au NP heterodimers under specified conditions, as well as for 40 nm AuNP monomers. The number of trajectories for each condition after removing outliers that deviate more than three scaled MAD from the median is (from left to right): 94, 116, 116, 123, 27. The heterodimer data was collected from at least five different batches. (B) *P*-value heatmap for a two-tailed Student's *T*-test. (C) Geometric model of the accessible volume (gray shaded area) for the pre-miRNA heterodimer to explore. The red circle indicates the 40 nm Au NP. The green circle indicate a shell of surface grafted single stranded DNA. The blue circle indicates the 20 nm Ag NP. (D) Same as in (C) but for post-miRNA accessible volume.

data is consistent with one sub-population whose MAD increases due to miRNA binding and a second fraction of dimers that do not change after miRNA addition because they either do not bind miRNA or are non-functional. 40 nm Au NP monomers and heterodimers post-spermidine show tight MAD distributions with averages that lie below those of all other dimer conditions. We also evaluated the coefficient of variance (COV) of the σ_{iSCAT} data as an additional measure for the contrast fluctuations that is normalized by the contrast mean (Fig. S8). The COV values confirm higher fluctuations for the post-miRNA condition. Although the Plasmon Ruler assembly conditions were chosen to optimize single tether formation with $\sim$8 tether molecules per 20 nm Au NP, some multivalent binding may occur. The resulting heterogeneity in the number of tethers between individual Plasmon Rulers may account for some of the spread in the MAD data.

Histograms of the average σ_{iSCAT}, values for the investigated experimental conditions are summarized in Fig. S9. The iSCAT contrast values are broadly distributed for the investigated Plasmon Ruler conditions, but the mean of the average contrast distribution of the heterodimers is significantly higher than that of the monomers and further increases for the post-spermidine condition.

The observation of higher MAD values of the iSCAT contrast σ_{iSCAT} for heterodimers than for monomers or for heterodimers with collapsed DNA tether after spermidine addition agrees with the model that structural fluctuations in DNA-linked NPs with intact DNA modulate the iSCAT contrast. To understand the increase in MAD for the post-miRNA case relative to the pre-miRNA and post-NCmiRNA conditions, we first take a closer look at the structure of the heterodimer and inspect the molecular details of the tether. The DNA handles are linked to the Au NP *via* a thiol terminated carbon chain of three or six carbon atoms. Given the flexibility of the carbon chain and the presence of flexible junctions (nicks) between double-stranded regions of the DNA linker (Fig. 1), the tethered 20 nm NP is free to explore a spherical sector around a pivot point that is defined by the thiol bond of handle 1 to the 40 nm Au NP surface. Assuming that the 20 nm Au NP cannot approach the 40 nm closer than 8.3 nm due to a shell of surface-grafted single-stranded DNA, a simple geometric model predicts that the 20 nm Au NP can explore a sector with an opening angle of

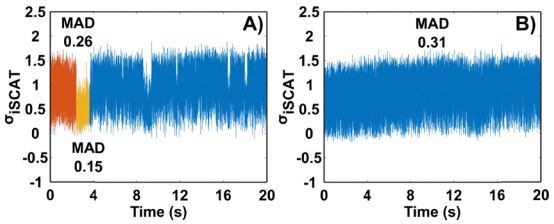

Fig. 5 (A) iSCAT contrast σ_{iSCAT} as function of time of a heterodimer plasmon ruler in T50 buffer that shows segments of different average contrast. (B) iSCAT contrast σ_{iSCAT} of a comparable heterodimer plasmon ruler in T50 buffer without distinct segments with different averages. All data shown are 50 points sliding averages.

122.8° before and 143.3° after miRNA binding (Fig. 4C and D). This change in opening angle together with an increased end-to-end length leads to an increase in accessible volume by a factor of approximately 1.6. The increase in conformational results in a larger number of interparticle separations and orientations relative to the immobilized 40 nm Au NP accessible to the tethered 20 nm Au NP and gives rise to a higher variability of the scattering signal and phase (Fig. 3). The additional increase in MAD observed for the post-miRNA case is thus consistent with a miRNA binding induced increase in conformational variability of the tether resulting in increased fluctuations of the iSCAT contrast.

A subset of σ_{iSCAT} trajectories of heterodimer plasmon rulers (~15%) exhibited systematic changes in average contrast as a function of time. This is exemplified with the two $\sigma_{iSCAT}(t)$ trajectories shown in Fig. 5, where only the trajectory in (A) shows distinct segments with different average contrast values. The trajectory in (B) lacks any indications for distinct regions characterized by different structural dynamics. The first 2 seconds for the trajectory in Fig. 5A show large amplitude contrast fluctuations centered around σ_{iSCAT} = 0.92. Subsequently, the contrast drops to an average σ_{iSCAT} = 0.42 for the next second or so. These two distinct states have MAD values of 0.26 and 0.15, respectively. Throughout the rest of the 20 s long trajectory the heterodimer transitions between these two different contrast levels for different durations, although the higher contrast is preferred. The reversible transition between two different contrast levels with different MAD values indicates two discrete minima in the energy landscape of the heterodimer that the system explores at different points in times. These could be related to interactions of the DNA tether with other surface groups or some residual rotational mobility of the surface-bound 40 nm Au NP that leads to changes in the orientation of the dimer axis.

Although the heterodimers used in this study did not exhibit significant differences in average σ_{iSCAT} in response to miRNA binding (Fig. S9), presumably due to a modest change of a relatively long tether (from 14.6 nm to 17.2 nm), it is conceivable to design heterodimer Plasmon Rulers with a shorter total tether length that undergo a detectable, non-reversible change in σ_{iSCAT} upon target analyte binding. In these constructs the conformational fluctuation analysis for the detection of analyte binding events, which is the focus of this work, could be

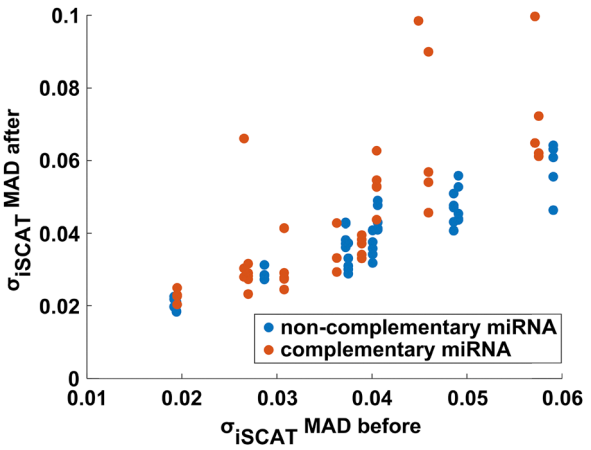

Fig. 6 MAD measured after addition of a 0.1 nM miRNA solution with complementary (miRNA) or noncomplementary (NCmiRNA) sequence as function of the initial MAD before addition of miRNA for individual Plasmon Rulers. The maximum incubation time was 20 min.

augmented by screening for systematic changes in average σ_{iSCAT}.

Up to this point, we only presented data recorded with an input concentration for 100 nM miRNA. To check whether detection of lower concentrations is feasible, we monitored the fluctuations for individual AuNP heterodimers before and up to 20 min after addition of complementary miRNA (post-miRNA) at a concentration of 0.1 nM. The same experiment was performed with the NC-miRNA control. The MAD of σ_{iSCAT} measured after addition of miRNA for both conditions is plotted as function of the initial MAD in Fig. 6. After addition of non-complementary miRNA the measured MAD values are almost identical do those measured before addition of miRNA. In contrast, addition of complementary miRNA results for some Plasmon Rulers in a strong increase in MAD values, which is indicative of miRNA binding.

Conclusions

iSCAT fluctuation microscopy of Plasmon Rulers detects changes in the conformational dynamics of the tether that are associated with plasmon coupling induced variations of the scattering cross-section and phase. We used this approach to examine 40 nm/20 nm Au NP heterodimer Plasmon Rulers containing a molecular beacon like recognition sequence in the tether before and after addition of target miRNA. Significant differences in the iSCAT contrast fluctuations after addition of the 22 nucleotides long target miRNA provide evidence of a change in the tether dynamics due to a miRNA binding induced opening of the hairpin motif. The heterodimer architecture in combination with iSCAT detection facilitates a decrease in the size of the NP performing a tethered particle motion in Plasmon Ruler assays and thus minimizes steric and excluded volume effects and provides new opportunities for characterizing the structural dynamics of individual biomolecules. The relatively high temporal resolution of iSCAT fluctuation

microscopy combined with the long observation time enabled by Plasmon Rulers makes it possible to explore both low and less probable high energy conformations of individual tether molecules and how they change as function of time or external stimuli. One aspect of particular interest is the kinetics of binding interactions between tether and binding molecules and the accompanying structural changes in the tether. It is, however, also clear that the miRNA used in this work to trigger the detected conformational switch in the Plasmon Ruler tether is an important sensing target due its important regulatory function.[46,47] Heterodimer Plasmon Rulers with a miRNA-recognizing DNA tether may provide a detection platform that complements conventional fluorescence-based molecular beacon approaches.[34–36] However, to realize this potential in real world sensing applications, integration of Plasmon Rulers into a microfluidic platform and increased optical throughput in large field of views need to be implemented. Furthermore, although the successful detection of miRNA analyte whose mass lies below the detection limit of iSCAT-based mass photometry[48–50] underlines the potential of iSCAT fluctuation microscopy of heterodimer Plasmon Rulers for detecting analytes with relatively low molecular weight, sensing applications require a further optimization of the Plasmon Ruler design. The changes in the conformational dynamics of the heterodimer investigated in this work are associated with a change in DNA tether end-to-end length of $\sim$2.6 nm, corresponding to a fractional change of $\sim$18%. The performance of heterodimer Plasmon Ruler ''molecular beacon'' sensors could be further improved by shortening the overall tether length to increase both the coupling between the NPs and the relative change in length upon target binding.

We close by stating that this work also motivates further studies into the nature of the observed iSCAT contrast fluctuations. In particular, studies using on and off-resonant excitation wavelengths are of especial interest for evaluating the contributions of plasmon coupling. Furthermore, investigations of homo- and heterodimer assemblies of different NP sizes promise additional insights into the contributions of plasmon coupling to experimentally observed iSCAT contrast fluctuations under resonant excitation conditions as function of NP size.

Methods

Materials

The following materials were used as obtained from the vendors: bis(*p*-sulfonatophenyl)phenylphosphine dihydrate dipotassium salt (BSPP) (Sigma-Aldritch), tris(2-carboxyethyl)phosphine (TCEP) (Sigma-Aldritch), 1 M tris(hydroxymethyl)aminomethane 2-amino-2-(hydroxymethyl)-1,3-propanediol (Tris buffer) (Sigma-Aldritch), SH-PEG-COOH 400 DA (NanoCS Inc.) All nucleotide sequences were purchased from Integrated DNA Technologies.

Assembly of DNA tethered Au NP dimers

Citrated-capped Au NP monomers were synthesized *via* the Turkevich method.[51] The citrate was then exchanged for BSPP by dissolving 1 mg mL^{-1} BSPP in an Au NP colloid solution overnight@45 °C in a water bath to improve the efficiency of DNA functionalization of Au NPs.[6] 1 mL aliquots of the Au/BSPP solution were transferred into Eppendorf DNA LoBind microcentrifuge tubes, centrifuged for 10 minutes at 5.0 (×1000)*g* for 40 nm Au NP or 10.0 (×1000)*g* for 20 nm Au NP. The supernatant was then removed, and the pellets were resuspended in 50 μL T20 (10 mM Tris buffer, pH 8.0 and 20 mM NaCl). Handle 1, handle 2, and biotin-functionalized DNA sequences (100 μM in Tris pH 8.0, 10 mM) were thawed and incubated with 10 mM TCEP in equal parts for 2 hours. The nucleotide sequences are shown in Table 1 with the molecular beacon hairpin underlined.

The Au NPs were then split into two batches to be functionalized with different DNA handle sequences. 7 μL of handle 1/TCEP solution and 3 μL of biotin-functionalized DNA/TCEP were incubated with the 40 nm Au NP solution (9×10^{10} NPs per mL) overnight at room temperature, and 10 μL of handle 2/TCEP was incubated with the 20 nm Au NP solution (7×10^{11} NPs per mL) overnight at room temperature. The next day 1 μL of 2 M NaCl was added to each Au NP solution and left to incubate overnight at room temperature to allow for increased DNA coverage of the Au NP surface. 1 μL of 10 mM 400 DA SH–PEG–COOH solution was then added to each Au NP solution and incubated overnight at room temperature to stabilize the particles. Excess DNA and PEG were subsequently removed by diluting the samples to 500 μL with DI water and centrifuging the particles in 50 kD MWCO centrifugal filters at 14.0 (×1000) rpm for 10 minutes. The filtrate was discarded, and the centrifugation process was repeated one more time to ensure the removal of all excess DNA and PEG. The concentrated solute was then recovered in a clean microcentrifuge tube by centrifuging the sample at 1.0 (×1000) rpm for 2 minutes. The concentrated Au NP solution was diluted to 1 mL in T90 (10 mM Tris buffer, pH 8.0 and 90 mM NaCl) buffer and centrifuged at the appropriate speed for 40 or 20 nm Au NPs for 10 minutes. 950 μL of the supernatant was removed and the handle 2 solution was incubated with 5 μL of 2 μM molecular

Table 1 Nucleic acid sequences

Handle 1	TGAACAAATGACATAGCCAGAAAAAAAAAA/3ThioMC3-D/
Handle 2	/5ThioMC6-D/AAAAAAAAAAGGCGGAAGAAATGTGTAAGG
Biotin-functionalized DNA	/5ThioMC6-D/AAAAAAAAAAGACCTACTAAGACTACTACACAACCAGAGA/3Bio/
Molecular beacon	CTGGCTATGTCATTTGTTCAATTTTTTTTTTTTTTTTTTTGGTCCTGCGCCCGCGCGCTAGCACTCGCCTTCA TTTTTTTTTTTTTTTTTTTTTCCTTACACATTTCTTCCGCC
miRNA 574-3P	CACGCrUCArUGCACACACCCACA
(non comple-mentary) miRNA control	GCAACGArUAGCrUGGCAACGAGC

beacon DNA overnight at room temperature. Preps containing handle 1 and handle 2 were combined and the NaCl was added to bring the buffer to 250 mM NaCl and annealed in a 70 °C waterbath for 10 minutes and left overnight at room temperature. The outlined conditions correspond to a AuNP : DNA ratio of 1 : 2344 for the 40 nm AuNP and handle 1, 1 : 1003 for 40 nm AuNP to biotin handle, 1 : 430 for 20 nm AuNP to handle 2, and 1 : 8.5 for 20 nm AuNP to molecular beacon sequence containing DNA linker. To separate the dimers from unreacted monomers and larger aggregates, gel electrophoresis was performed with a 1% agarose gel run at 120 V for 60 minutes. The dimer band was then recovered from the gel and placed in 200 μL T50 (10 mM Tris buffer, pH 8.0 and 50 mM NaCl) buffer to diffuse out of the gel overnight at room temperature.

iSCAT sample preparation

250 μL of a solution of BSA biotin (1 mg mL^{-1} in T50 pH 8), which had been filtered through a 0.22 μm filter was drop-cast on a glass slide and incubated for ten minutes. The glass slide was then washed with T50 buffer twice before being incubated with 250 μL NeutrAvadin (0.01 mg mL^{-1}) that had also been filtered through a 0.22 μm filter. The glass slide was then washed twice again before being incubated with 20 μL of the Au NP dimers in 250 μL T50 buffer for 10 minutes. The sample was then washed three times with T50 buffer to remove any dimers that were not immobilized on the surface.

Data collection

All data was collected using a home-built iSCAT microscope (Fig. S4). A 520 nm laser diode (lasertak) was spatially filtered through a 4F system, circularly polarized by a quarter-wave plate (Newport) and injected into a 100× oil objective 1.3NA (Olympus, UPLFLN100XO2) through a 50 : 50 beamsplitter with anti-reflective coating (Thorlabs). Laser radiation is dangerous, avoid eye or skin exposure. The scattered and reflected light in the sample plane was collected using the same objective. The collected light was split by a 70 : 30 beamsplitter (Thorlabs) to send 30% of the signal to a Mako G-234C CMOS camera (Allied Vision) and 70% of the light towards a photon detection module (PDM, Micro photon devices) for data collection. The sample was mounted on a Tritor102 nano positioner (Piezo-Jena), which was used with the CMOS camera to center the point-spread-function of individual scatterers on the PDM detector. A manual stage was used to explore the substrate for NP scatterers. Dimers were identified through iSCAT signal fluctuations on the CMOS camera recording at 200 frames per second. Once a scatterer was found using the CMOS camera, the nanopositioner was then used to raster scan the object with 0.25 nm step sizes and 50 ms integration time per step. iSCAT contrast and variance maps were generated and used to position the center of the point-spread-function on the PDM detector using LabVIEW. Subsequently, 20 s time trajectories were collected with a sampling rate of 50 kHz. The scatterer was then moved off the PDM to collect a corresponding background trajectory. Post-miRNA and post-NCmiRNA data was collected after incubating 20 μL of 100 nM miRNA in RNAse-free T90 buffer for 5 minutes with the dimers already immobilized on the glass slide and subsequently washed with T50 twice before data collection. All data was collected within 3.5 hours of thawing the miRNA to attempt to avoid miRNA degradation affecting the data. Post-spermidine samples were collected after incubating 20 μL of 10 mM spermidine in nanopure water with the sample for 1 minute. iSCAT contrast values were calculated according to eqn (3) using the median of the background trajectory as the reference intensity. Post-processing and analysis codes are available in the accompanying Zenodo deposition.

Conflicts of interest

No conflict of interest to declare.

Data availability

The raw iSCAT data, SEM images and Matlab analysis scripts for this article are available at Zenodo at https://doi.org/10.5281/zenodo.17594335.

Supplementary information: pair polarizability model, WLC model, photothermal effect evaluation, simulated optical spectra for 20 nm Au NP, UV-vis spectra, gel images for 40 nm/20 nm Au NP heterodimer assembly with TEM image, scheme of optical set-up, raw intensity trajectories, PSD plot for heterodimer post-spermidine, PSD plot for monomer pre-miRNA and dimer pre-miRNA and post-spermidine; COVs and mean iSCAT contrast values for investigated conditions, DLS data. See DOI: https://doi.org/10.1039/d5nh00763a

Acknowledgements

BMR acknowledges support from the National Science Foundation through grant CBET-2344525.

References

1 C. Sönnichsen, B. M. Reinhard, J. Liphardt and A. P. Alivisatos, A Molecular Ruler Based on Plasmon Coupling of Single Gold and Silver Nanoparticles, *Nat. Biotechnol.*, 2005, **23**(6), 741–745, DOI: 10.1038/nbt1100.

2 C. Tabor, R. Murali, M. Mahmoud and M. A. El-Sayed, On the Use of Plasmonic Nanoparticle Pairs As a Plasmon Ruler: The Dependence of the Near-Field Dipole Plasmon Coupling on Nanoparticle Size and Shape, *J. Phys. Chem. A*, 2009, **113**(10), 1946–1953, DOI: 10.1021/jp807904s.

3 R. T. Hill, J. J. Mock, A. Hucknall, S. D. Wolter, N. M. Jokerst, D. R. Smith and A. Chilkoti, Plasmon Ruler with Angstrom Length Resolution, *ACS Nano*, 2012, **6**(10), 9237–9246, DOI: 10.1021/nn3035809.

4 S. E. Lee, Q. Chen, R. Bhat, S. Petkiewicz, J. M. Smith, V. E. Ferry, A. L. Correia, A. P. Alivisatos and M. J. Bissell, Reversible Aptamer-Au Plasmon Rulers for Secreted Single Molecules, *Nano Lett.*, 2015, **15**(7), 4564–4570, DOI: 10.1021/acs.nanolett.5b01161.

5 B. M. Reinhard, M. Siu, H. Agarwal, A. P. Alivisatos and J. Liphardt, Calibration of Dynamic Molecular Rulers Based on Plasmon Coupling between Gold Nanoparticles, *Nano Lett.*, 2005, **5**(11), 2246–2252, DOI: 10.1021/nl051592s.

6 S. Lerch and B. M. Reinhard, Quantum Plasmonics: Optical Monitoring of DNA-Mediated Charge Transfer in Plasmon Rulers, *Adv. Mater.*, 2016, **28**(10), 2030–2036, DOI: 10.1002/adma.201503885.

7 L. Yang, H. Wang, B. Yan and B. M. Reinhard, Calibration of Silver Plasmon Rulers in the 1–25 Nm Separation Range: Experimental Indications of Distinct Plasmon Coupling Regimes, *J. Phys. Chem. C*, 2010, **114**(11), 4901–4908, DOI: 10.1021/jp911858v.

8 P. K. Jain, W. Huang and M. A. El-Sayed, On the Universal Scaling Behavior of the Distance Decay of Plasmon Coupling in Metal Nanoparticle Pairs: A Plasmon Ruler Equation, *Nano Lett.*, 2007, **7**(7), 2080–2088, DOI: 10.1021/nl071008a.

9 T. Chen, Y. Hong and B. M. Reinhard, Probing DNA Stiffness through Optical Fluctuation Analysis of Plasmon Rulers, *Nano Lett.*, 2015, **15**(8), 5349–5357, DOI: 10.1021/acs.nanolett.5b01725.

10 T. Chen, X. Wang, M. H. Alizadeh and B. M. Reinhard, Monitoring Transient Nanoparticle Interactions with Liposome-Confined Plasmonic Transducers, *Microsyst. Nanoeng*, 2017, **3**(1), 16086, DOI: 10.1038/micronano.2016.86.

11 W. Ye, M. Götz, S. Celiksoy, L. Tüting, C. Ratzke, J. Prasad, J. Ricken, S. V. Wegner, R. Ahijado-Guzmán, T. Hugel and C. Sönnichsen, Conformational Dynamics of a Single Protein Monitored for 24 h at Video Rate, *Nano Lett.*, 2018, **18**(10), 6633–6637, DOI: 10.1021/acs.nanolett.8b03342.

12 R. E. Armstrong, M. Horáček and P. Zijlstra, Plasmonic Assemblies for Real-Time Single-Molecule Biosensing, *Small*, 2020, **16**(52), 202003934, DOI: 10.1002/smll.202003934.

13 E. W. A. Visser, M. Horáček and P. Zijlstra, Plasmon Rulers as a Probe for Real-Time Microsecond Conformational Dynamics of Single Molecules, *Nano Lett.*, 2018, **18**(12), 7927–7934, DOI: 10.1021/acs.nanolett.8b03860.

14 L. V. Brown, H. Sobhani, J. B. Lassiter, P. Nordlander and N. J. Halas, Heterodimers: Plasmonic Properties of Mismatched Nanoparticle Pairs, *ACS Nano*, 2010, **4**(2), 819–832, DOI: 10.1021/nn9017312.

15 D. E. Segall, P. C. Nelson and R. Phillips, Volume-Exclusion Effects in Tethered-Particle Experiments: Bead Size Matters, *Phys. Rev. Lett.*, 2006, **96**(8), 088306, DOI: 10.1103/PhysRevLett.96.088306.

16 H. R. C. Dietrich, Tethered Particle Motion Mediated by Scattering from Gold Nanoparticles and Darkfield Microscopy, *J. Nanophoton*, 2009, **3**(1), 031795, DOI: 10.1117/1.3174445.

17 D. T. Kovari, Y. Yan, L. Finzi and D. Dunlap, Tethered Particle Motion: An Easy Technique for Probing DNA Topology and Interactions with Transcription Factors, in *Methods in Molecular Biology*, Springer New York, New York, NY, 2018, pp. 317–340. , DOI: 10.1007/978-1-4939-7271-5_17.

18 M. Manghi, C. Tardin, J. Baglio, P. Rousseau, L. Salomé and N. Destainville, Probing DNA Conformational Changes with High Temporal Resolution by Tethered Particle Motion, *Phys. Biol.*, 2010, **7**(4), 046003, DOI: 10.1088/1478-3975/7/4/046003.

19 M. Liu, J. Chao, S. Deng, K. Wang, K. Li and C. Fan, Dark-Field Microscopy in Imaging of Plasmon Resonant Nanoparticles, *Colloids Surf., B*, 2014, **124**, 111–117, DOI: 10.1016/j.colsurfb.2014.06.001.

20 S. Lerch and B. M. Reinhard, Effect of Interstitial Palladium on Plasmon-Driven Charge Transfer in Nanoparticle Dimers, *Nat. Commun.*, 2018, **9**(1), 1608, DOI: 10.1038/s41467-018-04066-2.

21 L. Velasco, A. N. Islam, K. Kundu, A. Oi and B. M. Reinhard, Two-Color Interferometric Scattering (iSCAT) Microscopy Reveals Structural Dynamics in Discrete Plasmonic Molecules, *Nanoscale*, 2024, **16**(24), 11696–11704, DOI: 10.1039/D4NR01288G.

22 V. Jacobsen, P. Stoller, C. Brunner, V. Vogel and V. Sandoghdar, Interferometric Optical Detection and Tracking of Very Small Gold Nanoparticles at a Water-Glass Interface, *Opt. Express*, 2006, **14**(1), 405, DOI: 10.1364/opex.14.000405.

23 R. W. Taylor and V. Sandoghdar, Interferometric Scattering Microscopy: Seeing Single Nanoparticles and Molecules via Rayleigh Scattering, *Nano Lett.*, 2019, **19**(8), 4827–4835, DOI: 10.1021/acs.nanolett.9b01822.

24 J. Ortega-Arroyo and P. Kukura, Interferometric Scattering Microscopy (iSCAT): New Frontiers in Ultrafast and Ultrasensitive Optical Microscopy, *Phys. Chem. Chem. Phys.*, 2012, **14**(45), 15625, DOI: 10.1039/c2cp41013c.

25 B.-K. Wu, S.-F. Tsai and C.-L. Hsieh, Simplified Interferometric Scattering Microscopy Using Low-Coherence Light for Enhanced Nanoparticle and Cellular Imaging, *J. Phys. Chem. C*, 2025, **129**(10), 5075–5085, DOI: 10.1021/acs.jpcc.4c07989.

26 Y.-H. Lin, W.-L. Chang and C.-L. Hsieh, Shot-Noise Limited Localization of Single 20 Nm Gold Particles with Nanometer Spatial Precision within Microseconds, *Opt. Express*, 2014, **22**(8), 9159, DOI: 10.1364/OE.22.009159.

27 F. Reina, C. Eggeling and C. Lagerholm, High-Speed Interferometric Scattering Tracking Microscopy of Compartmentalized Lipid Diffusion in Living Cells, *ChemPhysChem*, 2025, **26**(21), e202400407, DOI: 10.1002/cphc.202400407.

28 N. S. Ginsberg, C.-L. Hsieh, P. Kukura, M. Piliarik and V. Sandoghdar, Interferometric scattering microscopy, *Nat. Rev. Methods Primers*, 2025, **5**(23), DOI: 10.1038/s43586-025-00391-1.

29 K. Lindfors, T. Kalkbrenner, P. Stoller and V. Sandoghdar, Detection and Spectroscopy of Gold Nanoparticles Using Supercontinuum White Light Confocal Microscopy, *Phys. Rev. Lett.*, 2004, **93**(3), 037401, DOI: 10.1103/PhysRevLett.93.037401.

30 S. Sridhar, M. E. Nikolov, E. K. Beutler, M. Knobeloch, B. Paranzino, K. L. Vernon, Y. Zhong, X. Ye, L. A. Baker, S. E. Skrabalak, D. J. Masiello and K. A. Willets, Scattering vs Interference in Interferometric Scattering Spectroscopy of

Plasmonic Nanoparticles, *J. Phys. Chem. Lett.*, 2025, **16**(18), 4410–4418, DOI: 10.1021/acs.jpclett.5c00261.

31 R. W. Taylor and V. Sandoghdar, Interferometric Scattering (iSCAT) Microscopy and Related Techniques, in *Biological and Medical Physics, Biomedical Engineering*, Springer International Publishing, Cham, 2019, pp. 25–65, DOI: 10.1007/978-3-030-21722-8_2.

32 Z. Shi, J. Huang, X. Huang, Y. Huang, L. Wu and Q. Li, Resonant Scattering Enhanced Interferometric Scattering Microscopy, *Nanoscale*, 2020, **12**(14), 7969–7975, DOI: 10.1039/C9NR10391K.

33 H. Lee, H. Park, G. J. Yeon and Z. H. Kim, Amplitude and Phase Spectra of Light Scattered from a Single Nanoparticle, *ACS Photonics*, 2022, **9**(9), 3052–3059, DOI: 10.1021/acsphotonics.2c00803.

34 M. B. Baker, G. Bao and C. D. Searles, In Vitro Quantification of Specific microRNA Using Molecular Beacons, *Nucleic Acids Res.*, 2012, **40**(2), e13–e13, DOI: 10.1093/nar/gkr1016.

35 Z. Yu, Y. Zheng, H. Cai, S. Li, G. Liu, W. Kou, C. Yang, S. Cao, L. Chen, X. Liu, Z. Wan, N. Zhang, X. Li, G. Cui, Y. Chang, Y. Huang, H. Lv and T. Feng, Molecular Beacon–Based Detection of Circulating microRNA-Containing Extracellular Vesicle as an α-Synucleinopathy Biomarker, *Sci. Adv.*, 2024, **10**(20), eadl6442, DOI: 10.1126/sciadv.adl6442.

36 S. Tyagi and F. R. Kramer, Molecular Beacons: Probes That Fluoresce upon Hybridization, *Nat. Biotechnol.*, 1996, **14**(3), 303–308, DOI: 10.1038/nbt0396-303.

37 D. Botequim, R. Oliveira-Silva, V. V. Serra, P. Zijlstra, D. M. D. F. Prazeres and P. M. R. Paulo, Nanoplasmonics for Enhanced Fluorescence Detection of Nucleic Acids: From Fundamentals to Boosting Cancer Management, *Advanced NanoBiomed Research*, 2025, **5**(2), 2400088, DOI: 10.1002/anbr.202400088.

38 J. N. Milstein and J. C. Meiners, Worm-Like Chain (WLC) Model, in *Encyclopedia of Biophysics*, Springer Berlin Heidelberg, Berlin, Heidelberg, 2013, pp. 2757–2760, DOI: 10.1007/978-3-642-16712-6_502.

39 T. Chiyomaru, S. Yamamura, S. Fukuhara, H. Hidaka, S. Majid, S. Saini, S. Arora, G. Deng, V. Shahryari, I. Chang, Y. Tanaka, Z. L. Tabatabai, H. Enokida, N. Seki, M. Nakagawa and R. Dahiya, Genistein Up-Regulates Tumor Suppressor MicroRNA-574-3p in Prostate Cancer, *PLoS ONE*, 2013, **8**(3), e58929, DOI: 10.1371/journal.pone.0058929.

40 R. M. Paiva, D. A. G. Zauli, B. S. Neto and I. S. Brum, Urinary microRNAs Expression in Prostate Cancer Diagnosis: A Systematic Review, *Clin Transl Oncol*, 2020, **22**(11), 2061–2073, DOI: 10.1007/s12094-020-02349-z.

41 S. Tatarano, T. Chiyomaru, K. Kawakami, H. Enokida, H. Yoshino, H. Hidaka, N. Nohata, T. Yamasaki, T. Gotanda, T. Tachiwada, N. Seki and M. Nakagawa, Novel Oncogenic Function of Mesoderm Development Candidate 1 and Its Regulation by MiR-574-3p in Bladder Cancer Cell Lines, *Int. J. Oncol.*, 2012, **40**(4), 951–959, DOI: 10.3892/ijo.2011.1294.

42 L. R. Skewis and B. M. Reinhard, Spermidine Modulated Ribonuclease Activity Probed by RNA Plasmon Rulers, *Nano Lett.*, 2008, **8**(1), 214–220, DOI: 10.1021/nl0725042.

43 V. A. Bloomfield, DNA Condensation by Multivalent Cations, *Biopolymers*, 1997, **44**(3), 269–282, DOI: 10.1002/(sici)1097-0282(1997)44:3%253C269::aid-bip6%253E3.0.co;2-t.

44 L. C. Gosule and J. A. Schellman, DNA Condensation with Polyamines, *J. Mol. Biol.*, 1978, **121**(3), 311–326, DOI: 10.1016/0022-2836(78)90366-2.

45 P. K. Jain and M. A. El-Sayed, Plasmonic Coupling in Noble Metal Nanostructures, *Chem. Phys. Lett.*, 2010, **487**(4–6), 153–164, DOI: 10.1016/j.cplett.2010.01.062.

46 C. M. Croce, Causes and Consequences of microRNA Dysregulation in Cancer, *Nat. Rev. Genet.*, 2009, **10**(10), 704–714, DOI: 10.1038/nrg2634.

47 C. A. Juźwik, S. Drake, Y. Zhang, N. Paradis-Isler, A. Sylvester, A. Amar-Zifkin, C. Douglas, B. Morquette, C. S. Moore and A. E. Fournier, MicroRNA Dysregulation in Neurodegenerative Diseases: A Systematic Review, *Prog. Neurobiol.*, 2019, **182**, 101664, DOI: 10.1016/j.pneurobio.2019.101664.

48 M. Dahmardeh, H. Mirzaalian Dastjerdi, H. Mazal, H. Köstler and V. Sandoghdar, Self-Supervised Machine Learning Pushes the Sensitivity Limit in Label-Free Detection of Single Proteins below 10 kDa, *Nat. Methods*, 2023, **20**(3), 442–447, DOI: 10.1038/s41592-023-01778-2.

49 E. D. B. Foley, M. S. Kushwah, G. Young and P. Kukura, Mass Photometry Enables Label-Free Tracking and Mass Measurement of Single Proteins on Lipid Bilayers, *Nat. Methods*, 2021, **18**(10), 1247–1252, DOI: 10.1038/s41592-021-01261-w.

50 R. Asor, D. Loewenthal, R. Van Wee, J. L. P. Benesch and P. Kukura, Mass Photometry, *Annu. Rev. Biophys.*, 2025, **54**(1), 379–399, DOI: 10.1146/annurev-biophys-061824-111652.

51 J. Turkevich, P. C. Stevenson and J. Hillier, A Study of the Nucleation and Growth Processes in the Synthesis of Colloidal Gold, *Discuss. Faraday Soc.*, 1951, **11**, 55, DOI: 10.1039/df9511100055.

